HAL open science

Stacking order and electronic band structure in MBE-grown trilayer WSe_2 films

Aymen Mahmoudi, Meryem Bouaziz, Niels Chapuis, Fabrice Oehler, Pavel Dudin, Davide Romanin, Gilles Patriarche, Julien Chaste, Fausto Sirotti, Xavier Wallart, et al.

To cite this version:

Aymen Mahmoudi, Meryem Bouaziz, Niels Chapuis, Fabrice Oehler, Pavel Dudin, et al.. Stacking order and electronic band structure in MBE-grown trilayer WSe_2 films. Physical Review B, 2024, 109 (11), pp.115437. 10.1103/PhysRevB.109.115437 . hal-04543233

HAL Id: hal-04543233

https://hal.science/hal-04543233v1

Submitted on 12 Apr 2024

HAL is a multi-disciplinary open access archive for the deposit and dissemination of scientific research documents, whether they are published or not. The documents may come from teaching and research institutions in France or abroad, or from public or private research centers.

L'archive ouverte pluridisciplinaire **HAL**, est destinée au dépôt et à la diffusion de documents scientifiques de niveau recherche, publiés ou non, émanant des établissements d'enseignement et de recherche français ou étrangers, des laboratoires publics ou privés.

Stacking order and electronic band structure in MBE-grown trilayer WSe_2 films

Aymen Mahmoudi,[1] Meryem Bouaziz,[1] Niels Chapuis,[2] Fabrice Oehler,[1] Pavel Dudin,[3] Davide Romanin,[1] Gilles Patriarche,[1] Julien Chaste,[1] Fausto Sirotti,[4] Xavier Wallart,[2] Jose Avila,[3] and Abdelkarim Ouerghi[1,*]

[1]*Université Paris-Saclay, CNRS, Centre de Nanosciences et de Nanotechnologies, 91120, Palaiseau, Paris, France*
[2]*Université Lille, CNRS, Centrale Lille, Junia, Université Polytechnique Hauts de France, UMR 8520-IEMN F59000 Lille, France*
[3]*Synchrotron SOLEIL, L'Orme des Merisiers, Départementale 128, 91190 Saint-Aubin, France*
[4]*Laboratoire de Physique de la Matière Condensée, CNRS, Ecole Polytechnique, Institut Polytechnique de Paris, 91120, Palaiseau, France*

(Received 18 January 2024; revised 21 February 2024; accepted 28 February 2024; published 29 March 2024)

Few-layer quantum materials, such as transition-metal dichalcogenides (TMDs), are paving the path to the design of high-efficiency devices in the field of microelectronics and optoelectronics. However, heterostructures of quantum materials coming from different families, while they would immensely broaden the range of possible applications, remain challenging. Here, we demonstrate the large-scale integration of compounds from two highly multifunctional families: the three-dimensional conventional semiconductor GaP and the two-dimensional TMD semiconductor WSe_2 which is particularly interesting in terms of its potential for electronic, spintronic, and photonics applications. We show that a $2H$-$2H$ (or $AA'A$) trilayer of WSe_2 can be grown by molecular-beam epitaxy (MBE) onto gallium phosphide (GaP) substrate. A sharp, high-quality WSe_2-GaP interface was confirmed by scanning high-resolution transmission electron microscopy and x-ray photoemission spectroscopy. We present a combined experimental and theoretical study of the structure of the valence band of trilayer WSe_2. Nanoangle-resolved photoemission spectroscopy and density-functional theory calculation show that trilayer electrons populate two distinct subbands associated with the K and Γ valleys, with effective masses along the ΓM direction about 0.27 and 0.5 m_e, respectively (m_e is the bare electron mass).

DOI: 10.1103/PhysRevB.109.115437

I. INTRODUCTION

Two-dimensional (2D) semiconducting transition-metal dichalcogenides (TMDs) are promising candidates for high-performance electronic and optoelectronic devices because they exhibit atomically sharp interfaces, atomic thickness, flexibility, and optical properties suitable for applications [1]. For example, WSe_2 is one of the most promising 2D TMDs for which the band structure is reported in both monolayer and bilayer phases [2]: it possesses strong spin-orbit coupling, has large carrier effective masses, and can be isolated down to a single layer, making it an attractive host for phenomena associated with strong spin-orbit and electron-electron interactions [3]. Beyond the monolayer limit, the TMDs' band structure becomes more complicated [4]. For most of the few layers of thickness TMDs, the locations of the band extrema and their dependence on controllable parameters like stacking order [5] or field-effect doping [6,7] remain open questions that can be answered only by combining experiment and theory [8]. However, as films of TMDs on typical substrates such as Si/SiO_2 are usually composed by isolated flake of variable thicknesses and stacking order next to each other, tracking these two properties in a momentum-resolved manner has proven to be challenging.

Chemical vapor deposition (CVD) is one of the most promising methods to synthesize TMD films, and the successful CVD growth of WSe_2 with controlled composition of $2H$, and $3R$ phases has been reported [9]. However, large-area epitaxial growth of continuous and seamless TMD films with low defect density is still a challenging issue. Molecular-beam epitaxy (MBE) has recently received increased attention as an alternative method. Because of its superiority in controlling the thickness and composition of epitaxial films [10–13], MBE has been expected to synthesize high-quality and large-area atomically thin TMD films [14–16]. Such controlled synthesis of wafer-scale WSe_2 films with a deterministic crystal phase and layering is particularly important for practical applications in innovative devices [17,18]. In addition, MBE-grown 2D semiconductors are often synthesized on conventional three-dimensional (3D) semiconductor substrates, which is of interest for hybrid 2D–3D electronic devices that would employ the advantages of both the established 3D semiconductors and unique properties of ultrathin 2D crystals. However, in the current state of the art, MBE-grown TMD layers typically exhibits a well-determined epitaxial alignment with the 3D substrate, but small grain sizes in the 2D crystal (few tens of nanometers). In this context, conventional angle-resolved photoemission spectroscopy (ARPES) measurements with spot size of 50 μm on MBE samples will typically average over several grains, which is likely to broaden the experimental full width at half maximum (FWHM) of the electronics bands [17]. In practice, this broadening obfuscates the fine details of the band structure, which are key to identify the particular stacking order of the 2D material. In order to uncover the intrinsic electronic properties of our particular WSe_2 stacking configuration, as obtained by MBE on commercial GaP(111)B substrate, nano-ARPES

*Corresponding author: abdelkarim.ouerghi@c2n.upsaclay.fr

 ©2024 American Physical Society

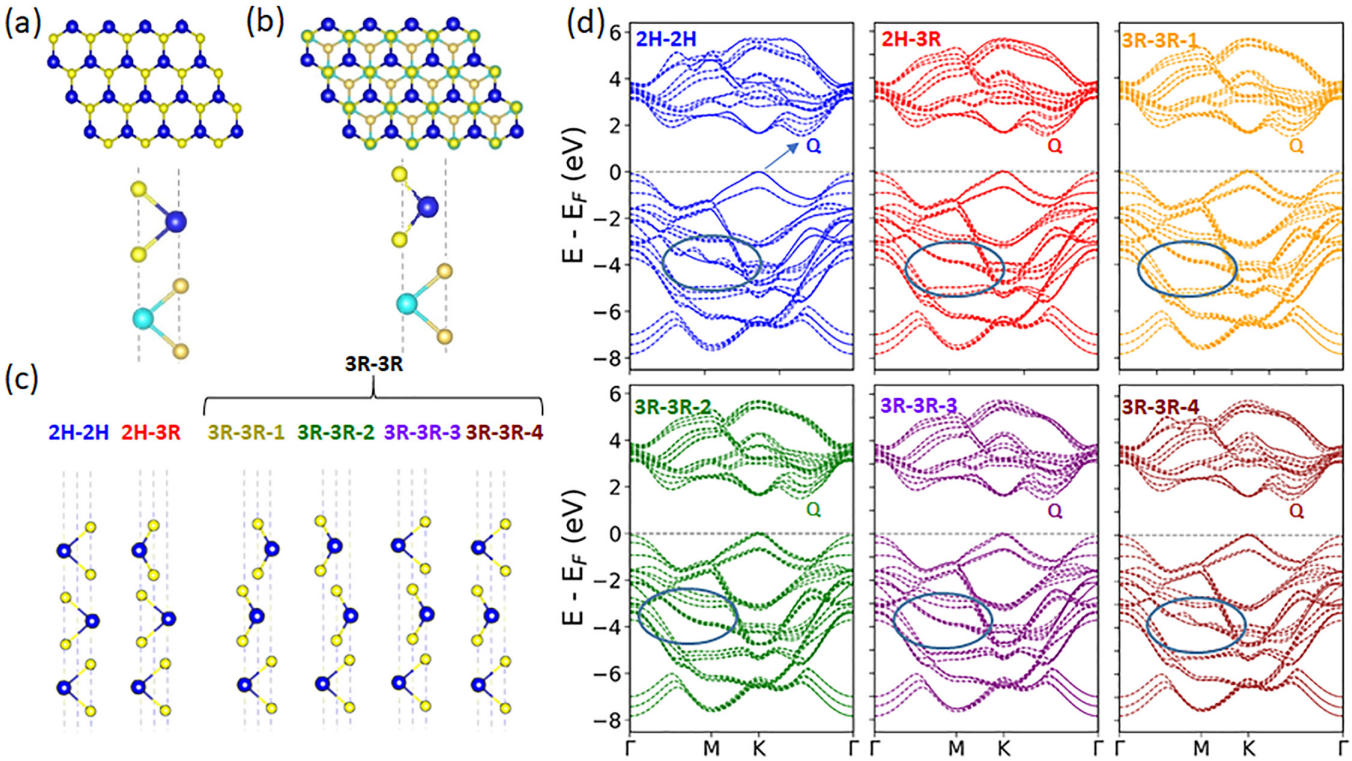

FIG. 1. Side views and electronic band structure (HSE hybrid functional with spin-orbit coupling) of trilayer WSe_2 with different stacking orders: (a), (b) Top and side views of the crystal structure for 2*H* and 3*R* bilayer cases, respectively. Yellow and blue balls denote Se and W atoms, respectively. (c) Trilayer stacking configurations 2*H*-2*H*, 2*H*-3*R*, 3*R*-3*R*-1 to 3*R*-3*R*-4. (d) Electronic band structure of 2*H*-2*H*, 2*H*-3*R*, 3*R*-3*R*-1 to 3*R*-3*R*-4, respectively. The Fermi level is set to top of valence band.

with small spot size (600 nm) is required [9]. Reducing the size of the beam spot reduces the number of integrated grains, which results in the decrease of the experimental FWHM of the electronics bands.

In this work, we present a direct measurement of the electronic band structure of a trilayer WSe_2 on a GaP(111)B substrate using nano-ARPES, combined with density-functional theory (DFT) calculations to determine its intrinsic electronic properties, such as the electrons populating two distinct subbands associated with the *K* and Γ valleys, the corresponding effective electronic mass (m^*), and the spin-orbit coupling (SOC). Using DFT calculations, we present the electronic band structure and the orbital projection band structure of several WSe_2 trilayers' stacking configurations. Then, we identify that our experimental trilayer WSe_2 exhibits a 2*H*-2*H* stacking order. Using nano-ARPES measurements, we also demonstrate that the quasi-freestanding electronic bands of our WSe_2 trilayer, as grown on GaP(111)B, lead to electrons populating two distinct subbands with different effective masses, 0.27 m_e and 0.5 m_e, at the *K* and Γ points respectively (where m_e is the bare electron mass).

II. RESULTS AND DISCUSSION

A. Crystal structure of trilayer WSe_2

The electronic properties of the few-layers TMDs [19] are strongly dependent on their stacking orders. Monolayer group-VI TMDs have a hexagonal lattice with a honeycomb structure: it is constructed by *X*–*M*–*X* (*X* = S, Se; *M* = Mo, W) triple atomic planes with strong in-plane interactions [18,20]. The most stable *H* phase of single-layer TMDs belongs to the *D*3*h* space group. Bilayer TMDs have two different stacking orders, as depicted in Figs. 1(a) and 1(b); the 2*H* (space group *P*63/*mmc*) and 3*R* (space group *R*3*m*). In both cases, the metal atoms have a trigonal prismatic coordination [21]. In the 2*H* stacking configuration, *M*(*X*) atoms reside directly above the *X*(*M*) atoms of another layer. The 3*R* stacking order contains three staggered layers; the *X* atoms in the middle layer are on top of the metal atoms of the bottom layer and under the hollow sites of the top layer [9]. Finally, trilayer WSe_2 has six high-symmetry stacking orders as detailed in Fig. 1(c): (i) 2*H*-2*H*, with both top–middle layers and middle–bottom layers being 2*H* stacking; (ii) 2*H*-3*R*, with bottom–middle layers having 2*H* stacking and middle–top layers having 3*R* stacking; and (iii) 3*R*-3*R*-1(2, 3, 4), with both the bottom–middle layers and middle–top layers stacked in 3*R* orders. Concerning the 3*R*-3*R* stacking orders, the difference lies in the relative orientations between the neighboring layers. In this case, we can name each structure according to stacking orders and constituent sequences.

Figure 1(d) shows the calculated electronic band structure for each polytype using Heyd Scuseria Ernzerhof (HSE) functionals with spin-orbit coupling; the band gap and band splitting at the *K* point of each layer are summarized in Table I. All of these stacking orders exhibit an indirect band gap. For trilayer WSe_2, the conduction-band minimum is located at the

TABLE I. Geometry parameters and electronic properties of the trilayer WSe_2 for the different stacking orders. d is the interplanar distances between the bottom–middle and middle–top layers, respectively. E_b is the corresponding cohesive energies for each stacking order. Δ_{SOC} indicates the VBM splitting at the K point in the bottom, middle, and top layers, respectively. The unit of energy is eV. The optimized lattice constant is $a = 3.32$ Å for all cases.

Stacking 2*H*-2*H*	d (Å)	Gap (eV)	Δ^k_{SOC} (eV)	E_b (meV)
2*H*-2*H*	3.214–3.214	1.48	0.66–0.00–0.00	0.0
2*H*-3*R*	3.215–3.214	1.43	0.70–0.05–0.00	4.0
3*R*-3*R*-1	3.215–3.215	1.37	0.76–0.07–0.03	7.0
3*R*-3*R*-2	3.215–3.215	1.37	0.75–0.06–0.05	7.1
3*R*-3*R*-3	3.215–3.215	1.39	0.73–0.07–0.00	7.3
3*R*-3*R*-4	3.215–3.215	1.41	0.70–0.06–0.00	5.8

Q (Q') points of the Brillouin zone (BZ), while the valence-band maxima are at K/K' and Γ. Consequently, the lowest exciton transition in trilayer WSe_2 should be momentum-indirect Q-K or Q-Γ excitons, in marked contrast to the momentum-direct K-K transition in the single-layer case. Although the overall dispersion looks nearly similar, there are differences between all polytypes, especially for the valence band near the M and K points, where the effect of the strong spin-orbit interaction and the reduced number of symmetries of the crystal structure play an important role. Particularly, comparing 2*H*-2*H* and 3*R*-3*R*-4 to the rest of the other band structures around the M point, we notice that the dispersion is almost identical, but the bands located at the M point [around −3.5-eV binding energy and circled in Fig. 1(d)] have different behaviors. Besides, 2*H*-2*H* to 3*R*-3*R*-4 all share the same band structure along the ΓK high-symmetry direction but disperse differently along KMK', clearly showing the effect of the stacking order directly on the dispersion of the bands.

By means of DFT, we calculated the total cohesive energies for the trilayer WSe_2 in the different possible stacking orders. Quantitatively, the computed energy values are summarized in Table I. Our results show that it is indeed the 2*H*-2*H* and 2*H*-3*R* stacking that presents the lowest total energy for the 3 ML (monolayers). Such calculations are very helpful in understanding the growth process through estimating the probability of growth of each phase.

B. Sharp interface and stacking-order trilayer WSe_2/GaP(111) heterostructure

For the growth of trilayer WSe_2, we use here commercial GaP(111)B substrates of size 1/6 of 2-inch wafer, which are thermally deoxidized under combined atomic hydrogen and cracked phosphine fluxes in a dedicated MBE chamber [22]. The MBE procedure for epitaxial growth of WSe_2 requires a Se preexposure of the GaP(111)B surface at high temperature (700 °C), prior to the WSe_2 deposition at 450 °C. This Se preexposure of the GaP(111)B is crucial for the correct quasi–van der Waals epitaxy WSe_2 on GaP(111)B substrate [see Figs. 2(a) and 2(b)]. Note that

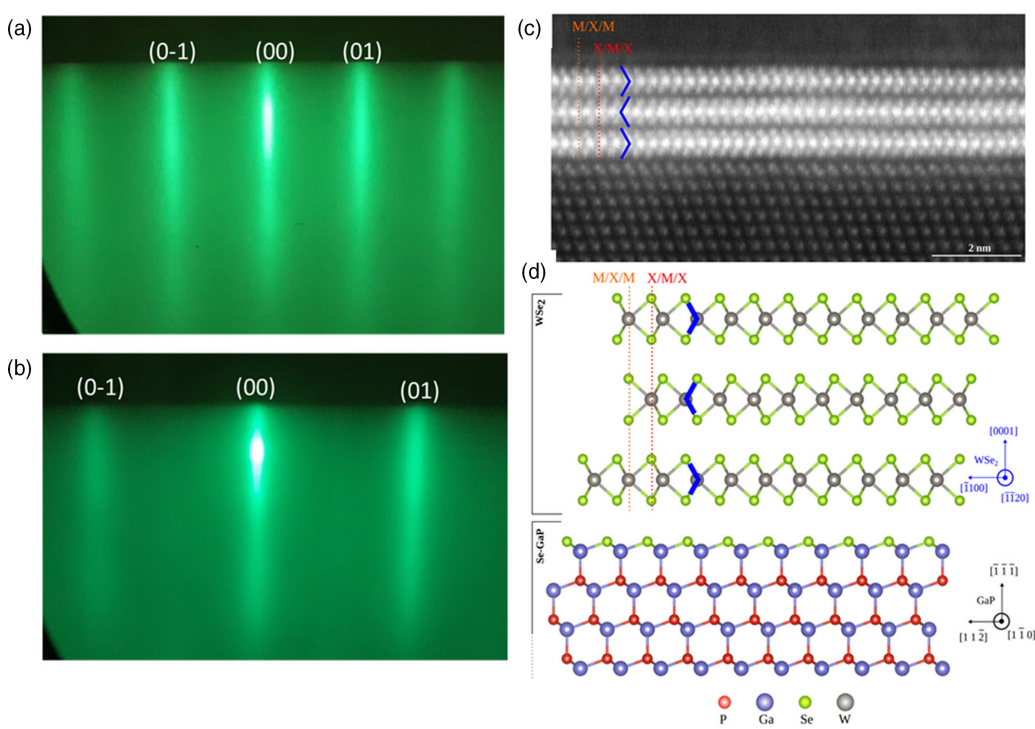

FIG. 2. Stacking order of the WSe_2/GaP(111) heterostructure: (a), (b) RHEED pattern of WSe_2/GaP(111) along the respective [11–20] and [1-100] azimuths of WSe_2, after annealing at 600 °C under Se flux. (c) High-resolution STEM image with the overlaid atomic structure of the 2*H*-2*H* stacking trilayer WSe_2. (d) Corresponding atomic structure of the 2*H*-2*H* stacking trilayer WSe_2 on the Se-treated GaP(111) surface.

this Se-preexposure of the GaP(111)B surface, prior to the growth, is different than final annealing under Se flux at 650 °C of the grown WSe_2 layers during 15 min. Figures 2(a) and 2(b) show reflection high-energy diffraction (RHEED) patterns taken after the final annealing of WSe_2 films on GaP(111)B under Se flux along two perpendicular azimuths. The appearance of the sharp elongated streaks in the RHEED patterns suggests a well-aligned crystal order and a flat surface of WSe_2 with the [11–20] WSe_2 direction being parallel to the GaP [1–10] direction. To study the interface and the stacking order of WSe_2/GaP(111) heterostructure, we have carried out measurement with scanning transmission electron microscopy (STEM). Figure 2(c) presents an atomically resolved STEM image acquired in the high-angle annular dark-field mode. In this mode, the large difference in average atomic number between GaP and WSe_2 produces high contrast between the WSe_2 trilayer and GaP(111) substrate. The WSe_2/GaP interface appears sharp and flat, without interdiffusion between the two materials. A larger-scale image is presented in Supplemental Material [23], Fig. S1, showing the same configuration across 70-nm lateral width. We note that the WSe_2 trilayer is fully oriented on the GaP(111) surface. We observe the following epitaxial relationship with $[11{-}20]_{WSe_2}//[1{-}10]_{GaP}$ and $[1{-}100]_{WSe_2}//[11{-}2]_{GaP}$ in the plane and $[0001]_{WSe_2}//[{-}1{-}1-1]_{GaP}$ out of plane. This relationship is confirmed by additional in-plane x-ray-diffraction measurements (see Supplemental Material [23], Fig. S2). The interlayer spacing between the two WSe_2 layers is (6.45 ± 0.10) Å, which is in very good agreement with the standard van der Waals (vdW) gap between consecutive layers in bulk hexagonal WSe_2 (6.48 Å) [24]. The vertical separation between the central W atoms of the first WSe_2 layer and the lower Ga atom is (6.20 ± 0.20) Å, which is consistent with a quasi-vdW gap between WSe_2 and GaP(111), as summarized in Fig. 2(d). Comparing the orientation of the Se–W–Se bonds between the upper, middle, and lower WSe_2 layers, we confirm the existence of the 2*H*-2*H* configuration in our sample.

C. Electronic band structure of trilayer WSe_2

The samples are capped with amorphous Se to protect them from surface oxidation between the MBE chamber and the nano-ARPES measurements. This capping is removed thermally prior to the x-ray photoemission spectroscopy (XPS) and ARPES measurements. The XPS spectra were recorded with photon energy $h\nu = 95$ eV and at temperature $T = 70$ K. XPS survey scan is shown in Supplemental Material [23], Fig. S3. The detailed spectra of W $4f$ and Se $3d$ core levels are shown in Figs. 3(a) and 3(b), respectively, both consisting of one spin-orbit doublet. W $4f_{7/2}$ and W $4f_{5/2}$ peaks are located at 32.3 and 34.4 eV, respectively, and the peak positions of Se $3d_{5/2}$ and Se $3d_{3/2}$ are 54.3 and 55.2 eV, respectively [8]. In both spectra, there is no signature of components at other binding energies that could be related to gallium, phosphor oxygen, or carbon bonded to W and/or Se atoms. This confirms that the grown WSe_2 crystals are obtained by van der Waals epitaxy and that no interdiffusion and oxidation of the sample take place.

The MBE growth process is performed in UHV to achieve a precise control of the number of TMDs layers. In current

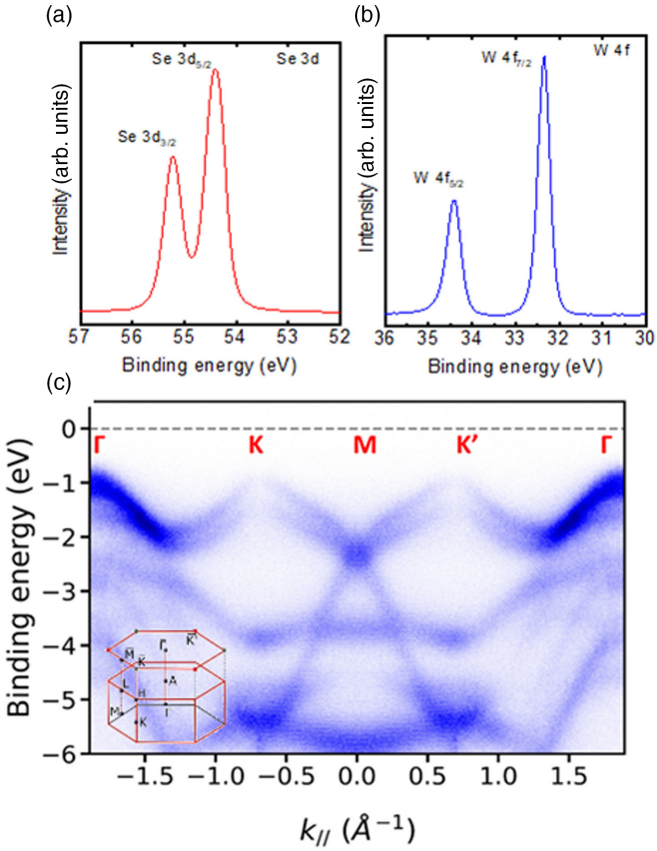

FIG. 3. Chemical properties of the WSe_2/GaP(111)B heterostructure: (a), (b) XPS core-level spectra of Se $3d$ and W $4f$, respectively, measured at $h\nu = 96$ eV. (c) Nano-ARPES measurements ($h\nu = 96$ eV, $T = 70$ K) of the electronic structure along the $\Gamma KMK'\Gamma$ high-symmetry directions. The Fermi-level position is located at the zero of the binding energy (marked by a gray dotted line).

state of the art, MBE-grown TMD layers typically consist show small grain sizes [25] of a few tens of nanometers, so that nano-ARPES is well suited to measure the intrinsic properties the material [SOC, the m^* of the WSe_2/GaP(111) heterostructure] [22]. Figure 3(c) show nano-ARPES data along the high-symmetry directions over the entire Brillouin zone ($h\nu = 96$ eV and temperature $T = 70$ K). This image shows that the valence-band maximum (VBM) is located at 0.8 eV below the Fermi level (E_F). The zero of binding energy (E_F) was determined by fitting the leading edge of the gold at the same photon energies and under the same experimental conditions. Isoenergy cuts (see Supplemental Material [23], Fig. S4) show that the *K* pockets exhibits hexagonal symmetry, which indicates that they originate from a single-orientation WSe_2 trilayer on the GaP(111) substrate. The presence of a single pocket at a unique well-determined *K* position in the plane further confirms that the WSe_2 film presents a single orientation, with a unique lattice alignment between the WSe_2 and the GaP(111) substrate, as determined by TEM (Fig. 2) and x-ray diffraction (Supplemental Material [23]). Combining the total valence-band mapping in the reciprocal space, and the spatial information in the real space, we map in Supplemental Material [23], Fig. S5 the spatial

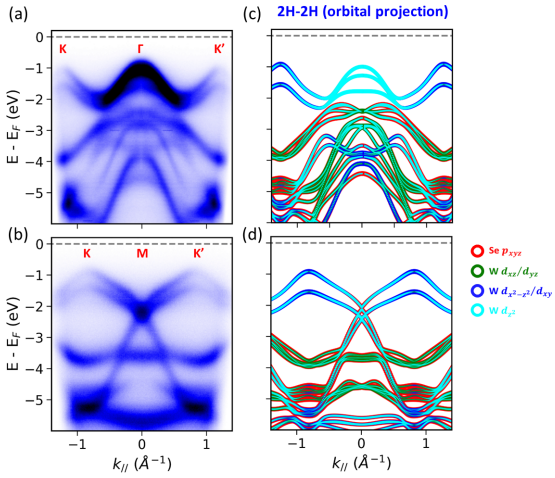

FIG. 4. Comparison between the experimental and orbital projection band structure of WSe_2/GaP(111): (a), (d) ARPES measurements of the valence band along the $K\Gamma K'$ and KMK' high-symmetry directions of WSe_2, respectively ($h\nu = 96$, $T = 70$ K). (c), and (d) Orbital projected band structure of the trilayer WSe_2. The energy scale is shifted to align with the experiments. The main projections on the composing orbitals are indicated with the colors shown on the right of panel.

homogeneity of the sample over 300 μm by, respectively, integrating the VBM at Γ, as well as the Se 3d and W 4f core levels. This confirms the large-scale homogeneity of our sample.

In Figs. 4(a) and 4(b), we present the ARPES measurement along the $K\Gamma K'$ and KMK' high-symmetry directions. The sharpness of the different bands indicates a high quality of the WSe_2 layer. Using density functional theory calculations of Fig. 1(c), we can unambiguously confirm the atomic orbital character of each band. For this, we added the $k-E$ maps of the 2*H*-2*H* stacking electronic band structures, uniformly shifting the Fermi level of the DFT data to match the experimental VBM [Figs. 4(c) and 4(d)]. We observe an agreement over all the investigated k space. The VBM is at Γ, indicating the indirect band-gap character of the trilayer WSe_2, in stark contrast with direct band-gap monolayer WSe_2. Detailed investigation of the valence band at Γ (see Supplemental Material [23], Fig. S6), shows that the VBM may be decomposed into three contributions at the Γ point, which reproduces the position of the calculated bands for WSe_2 of trilayer thickness. In the ARPES spectra, the distinctive features include the VBM at Γ, derived from the W d_{z^2} and Se p_z orbitals, the VBM at K point, derived from the W $d_{x^2-y^2}/d_{xy}$ and Se p_x/p_y orbitals, and the valley between Γ and K, derived from a crossover between the W $d_{x^2-y^2}/d_{xy}$ orbitals and the W d_{z^2} and Se p_z orbitals. Bands of higher binding energies and along other high-symmetry directions can also be identified. The distinctive features at the M point derived from the W $d_{x^2-y^2}/d_{xy}$ orbitals and Se p_z orbitals are well resolved. The valence bands at the K point of WSe_2 are resolved with excellent quality. They are consistent with the result of the first-principles calculation [Fig. 1(c)]. The large band splitting arising in the topmost WSe_2 valence band at K is clearly resolved in the ARPES data. To quantify this band splitting, an energy distribution curve (EDC) was extracted at the K point of WSe_2, as indicated by the dashed black line in Supplemental Material [23], Fig. S7. By fitting this EDC with two pseudo-Voigt curves, we obtain SOC $= 520 \pm 10$ meV. This value is slightly larger than the 513 meV observed in monolayer WSe_2 exfoliated from a bulk crystal [26] or obtained by CVD [8]. Overall this result confirms the absence of residual strain between WSe_2 on GaP(111) [27]. An analysis of the curvature of the bands from the nano-ARPES measurements also allows us to deduce the effective mass of trilayer WSe_2. For trilayer WSe_2, we determined an experimentally derived electron effective mass of $0.27\,m_e$ at K, and an electron effective mass of $0.5\,m_e$ at Γ, which agrees well with theoretical predictions.

Our DFT calculations show that it is indeed the 2*H*-2*H* and 2*H*-3*R* stacking that presents the lowest total energy for the three-layer WSe_2. Such calculations are very helpful in understanding the growth process through estimating the probability of existence for each phase. In order to compare the experimental data and identify the corresponding trilayer stacking, we superpose the $k-E$ maps of the calculated electronic band structures for the $K\Gamma K'$ and KMK' high-symmetry direction of the BZ [Figs. 5(a)–5(d)]. In Figs. 5(e) and 5(f), the calculated band structure for the two most stable configurations 2*H*-2*H* and 2*H*-3*R* are overlaid on the second derivative of the raw data. We observe an agreement over all the investigated k space and the main features are well reproduced by the calculated band structures along two high-symmetry directions. However, the calculated bands located at the M point (around −4.5-eV binding energy) have different behaviors. The width of the experimental data is clearly matching better with the calculated data resulting from the 2*H*-2*H* stacking around the M point at −4.5 eV. In Supplemental Material [23], Fig. S8, we superpose the $k-E$ maps of the calculated electronic band structures for the different stacking order. We can notice that specifically at the M point, the bands are wider for the 2*H*-2*H* and 3*R*-3*R*-4 stacking, whereas they are getting sharper for the other stackings, respectively. Since the valence-band structures of 2*H*-2*H* and 3*R*-3*R*-4 stacking are quite similar, one could think of attributing the trilayer WSe_2 electronic dispersion to the 3*R*-3*R*-4 stacking configuration. However, the cohesive energies between the bands is higher for 3*R*-3*R*-4 than for 2*H*-2*H*, which eliminates the possibility of the energetically unstable 3*R*-3*R*-4 stacking formation (Table I).

Finally, according to the comparison with the DFT calculation on trilayer freestanding WSe_2 and the STEM image [Fig. 2(b)], it seems that our trilayer WSe_2/GaP(111) hybrid heterostructure shares the same electronic dispersion as a freestanding 2*H*-2*H* trilayer WSe_2. Considering this agreement and the stability of the corresponding stacking, we confirm that the trilayer WSe_2 can be considered as quasi-freestanding on the GaP(111)B surface, with no interlayer hybridization. This indicates that trilayer WSe_2 is a promising candidate for the formation of a 2*H*-2*H* stacking order.

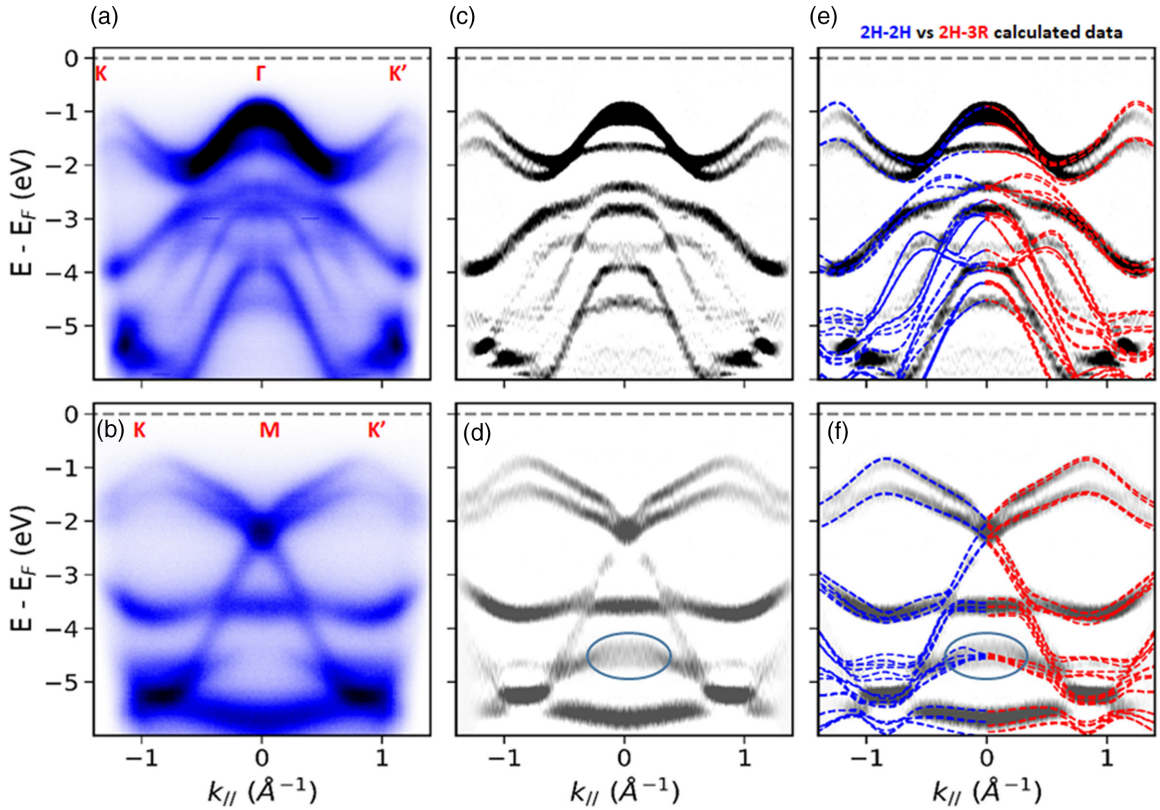

FIG. 5. Comparison of the band structure with the DFT data from 2*H*-2*H* and 2*H*-3*R* stacking: (a), (b) ARPES measurement of the trilayer WSe_2/GaP(111) structure along $K\Gamma K'$ and KMK'. (c), (d) The corresponding second derivative of the raw scans in (a) and (b), respectively. (e), (f) The calculated band structure overlaid on the second derivative picture in (c) and (d), respectively. The simulation is performed using a trilayer relaxed structure with a lattice parameter of 3.26 Å and an interlayer vacuum of 15 Å.

III. CONCLUSION

In summary, we demonstrated the molecular-beam epitaxial growth of hybrid trilayer WSe_2 on GaP(111)B heterostructure via quasi–van der Waals epitaxy. We have probed the surface structure and occupied electronic bands of three-layer WSe_2 on GaP(111) substrate. STEM and RHEED provided real and reciprocal-space structural measurements of WSe_2, revealing clearly resolved thickness and interface, respectively. Our nano-ARPES measurements have probed the valence-band structure and confirmed the 2*H*-2*H* stacking order of trilayer WSe_2. We have found an electron effective mass of 0.27 m_e at *K*, and an electron effective mass of 0.5 m_e at Γ. We expect that these results will provide insight for understanding the optical and electronic properties of trilayer WSe_2 that are important for devices made from this transition-metal dichalcogenide material.

IV. METHODS

A. Experimental growth of WSe_2 trilayer on Se-terminated GaP(111) substrate

Commercial GaP(111)B substrates (residual *n*-type doping $2-4.7 \times 10^{16}$ at. cm^{-3}) are cleaved into regular piece of 1/6 of 2-inch wafer to fit our various sample holders. The GaP(111)B is deoxidized under cracked phosphine and an atomic hydrogen flux by ramping the substrate temperature up to 540 °C in a dedicated III–V MBE reactor. The sample is then transferred under ultrahigh vacuum condition to another TMD-dedicated MBE reactor for Se passivation. The sample is heated up to 250 °C before being exposed to a Se flux, further annealed to 700 °C, and kept at this temperature for 3 min. Such arrangement displays a quasi–van der Waals character, which is particularly suitable for the subsequent growth of trilayer WSe_2 material. The WSe_2 growth is calibrated to obtain a final layer of 3-ML thickness. For this, the temperature of the Se-terminated GaP(111)B surface is ramped down and stabilized at 450 °C under the Se flux before being exposed to the W flux from an electron gun evaporator (Telemark model 575). Finally, the sample is annealed under Se only at 650°C.

B. Photoemission spectroscopy

The nano-ARPES experiments were performed at the ANTARES beamline of the SOLEIL synchrotron light source (Saint-Aubin, France). The nano-ARPES data were taken at a photon energy of 96 eV, using linearly polarized light. All ARPES measurements were carried out at a pressure of 10^{-10} mbar and at a temperature of 70 K.

C. DFT calculation

First-principles calculations were performed using the plane-wave pseudopotential method as implemented in the QUANTUM ESPRESSO package [28]. We employed

norm-conserving fully relativistic pseudopotentials for all atomic species, with an energy cutoff for the valence wave function of 60 Ry. Spin-orbit coupling effects on both the structural relaxation and the electronic dispersion were also considered by performing noncollinear calculations. Free-standing monolayers are modeled with ≈20 Å of vacuum between adjacent trilayers in the supercell in the nonperiodic direction (i.e., perpendicular to the surface) and van der Waals interaction were also considered via the Grimme (D3) corrections. Structural relaxation was performed via the Perdew-Burke-Ernzerhof [29] exchange-correlation functional and a Brillouin-zone integration on a uniform grid of $24 \times 24 \times 1$ k points. The final electronic band structure and energetics for identification of the most stable stacking were obtained through the Heyd-Scuseria-Ernzerhof 06 exchange-correlation functional [30] and a Brillouin-zone integration on a uniform grid of $6 \times 6 \times 1$ k points and a kinetic energy cutoff for the exact exchange operator of 120 Ry. In order to obtain the final band structure with hybrid functionals, Wannier interpolation has been performed using $p-(\mathrm{f}-)$ orbitals for Se (W) atoms.

ACKNOWLEDGMENTS

We thank Ir. Christophe Coinon for his help with the epitaxial growth and Ir. David Troadec for the Focused Ion Beam preparation of the STEM slabs. We acknowledge the financial support by DEEP2D (Grant No. ANR-22-CE09-0013), 2D-on-Demand (Grant ANR-20-CE09-0026), MixDferro (Grant No. ANR-21-CE09-0029), Tunne2D (Grant No. ANR-21-CE24-0030), TyLDE (Grant No. ANR-23-CE50-0001-01), ADICT (Grant No. ANR-22-PEEL-0011), and FastNano (Grant No. ANR-22-PEXD-0006) projects, as well as the French technological network RENATECH. D.R. acknowledges support from the HPC resources of IDRIS, CINES, and TGCC under Allocation No. 2023-A0140914101 made by GENCI.

The authors declare no conflicts of interest.

[1] C. R. Woods, L. Britnell, A. Eckmann, R. S. Ma, J. C. Lu, H. M. Guo, X. Lin, G. L. Yu, Y. Cao, R. V. Gorbachev, A. V. Kretinin, J. Park, L. A. Ponomarenko, M. I. Katsnelson, Yu. N. Gornostyrev, K. Watanabe, T. Taniguchi, C. Casiraghi, H.-J. Gao *et al.*, Commensurate–incommensurate transition in graphene on hexagonal boron nitride, Nat. Phys. **10**, 451 (2014).

[2] H. Nakamura, A. Mohammed, P. Rosenzweig, K. Matsuda, K. Nowakowski, K. Küster, P. Wochner, S. Ibrahimkutty, U. Wedig, H. Hussain, J. Rawle, C. Nicklin, B. Stuhlhofer, G. Cristiani, G. Logvenov, H. Takagi, and U. Starke, Spin splitting and strain in epitaxial monolayer WSe_2 on graphene, Phys. Rev. B **101**, 165103 (2020).

[3] M. M. Ugeda, A. Pulkin, S. Tang, H. Ryu, Q. Wu, Y. Zhang, D. Wong, Z. Pedramrazi, A. Martín-Recio, Y. Chen, F. Wang, Z.-X. Shen, S.-K. Mo, O. V. Yazyev, and M. F. Crommie, Observation of topologically protected states at crystalline phase boundaries in single-layer WSe_2, Nat. Commun. **9**, 3401 (2018).

[4] M. T. Dau, M. Gay, D. Di Felice, C. Vergnaud, A. Marty, C. Beigné, G. Renaud, O. Renault, P. Mallet, T. Le Quang, J. Y. Veuillen, L. Huder, V. T. Renard, C. Chapelier, G. Zamborlini, M. Jugovac, V. Feyer, Y. J. Dappe, P. Pochet *et al.*, Beyond van der Waals interaction: The case of $MoSe_2$ epitaxially grown on few-layer graphene, ACS Nano **12**, 2319 (2018).

[5] K. M. McCreary, M. Phillips, H. J. Chuang, D. Wickramaratne, M. Rosenberger, C. S. Hellberg, and B. T. Jonker, Stacking-dependent optical properties in bilayer WSe_2, Nanoscale **14**, 147 (2022).

[6] E. Piatti, D. Romanin, and R. S. Gonnelli, Mapping multi-valley Lifshitz transitions induced by field-effect doping in strained MoS_2 nanolayers, J. Phys.: Condens. Matter **31**, 114002 (2019).

[7] D. Romanin, T. Brumme, D. Daghero, R. S. Gonnelli, and E. Piatti, Strong band-filling-dependence of the scattering lifetime in gated MoS_2 nanolayers induced by the opening of intervalley scattering channels, J. Appl. Phys. **128**, 063907 (2020).

[8] C. Ernandes, L. Khalil, H. Almabrouk, D. Pierucci, B. Zheng, J. Avila, P. Dudin, J. Chaste, F. Oehler, M. Pala, F. Bisti, T. Brulé, E. Lhuillier, A. Pan, and A. Ouerghi, Indirect to direct band gap crossover in two-dimensional $WS_{2(1-x)}Se_{2x}$ alloys, npj 2D Mater. Appl. **5**, 7 (2021).

[9] A. Mahmoudi, M. Bouaziz, A. Chiout, G. Di Berardino, N. Ullberg, G. Kremer, P. Dudin, J. Avila, M. Silly, V. Derycke, D. Romanin, M. Pala, I. C. Gerber, J. Chaste, F. Oehler, and A. Ouerghi, Electronic properties of rhombohedrally stacked bilayer WSe_2 obtained by chemical vapor deposition, Phys. Rev. B **108**, 045417 (2023).

[10] Z. Ogorzalek, B. Seredynski, S. Kret, A. Kwiatkowski, K. P. Korona, M. Grzeszczyk, J. Mierzejewski, D. Wasik, W. Pacuski, J. Sadowski, and M. Gryglas-Borysiewicz, Charge transport in MBE-Grown 2H-$MoTe_2$ bilayers with enhanced stability provided by an AlO_x capping layer, Nanoscale **12**, 16535 (2020).

[11] S. Vishwanath, A. Sundar, X. Liu, A. Azcatl, E. Lochocki, A. R. Woll, S. Rouvimov, W. S. Hwang, N. Lu, X. Peng, H. H. Lien, J. Weisenberger, S. McDonnell, M. J. Kim, M. Dobrowolska, J. K. Furdyna, K. Shen, R. M. Wallace, D. Jena *et al.*, MBE growth of few-layer 2H-$MoTe_2$ on 3D Substrates, J. Cryst. Growth **482**, 61 (2018).

[12] Z. B. Aziza, D. Pierucci, H. Henck, M. G. Silly, C. David, M. Yoon, F. Sirotti, K. Xiao, M. Eddrief, J.-C. Girard, and A. Ouerghi, Tunable quasiparticle band gap in few layer GaSe/graphene van der Waals heterostructures, Phys. Rev. B **96**, 035407 (2017).

[13] Z. Ben Aziza, H. Henck, D. Pierucci, M. G. Silly, E. Lhuillier, G. Patriarche, F. Sirotti, M. Eddrief, and A. Ouerghi, van der Waals epitaxy of GaSe/Graphene heterostructure: Electronic and interfacial properties, ACS Nano **10**, 9679 (2016).

[14] P. Chen, W. W. Pai, Y.-H. Chan, W.-L. Sun, C.-Z. Xu, D.-S. Lin, M. Y. Chou, A.-V. Fedorov, and T.-C. Chiang, Large quantum-spin-Hall gap in single-layer 1T′ WSe_2, Nat. Commun. **9**, 2003 (2018).

[15] A. Ohtake and Y. Sakuma, Evolution of surface and interface structures in molecular-beam epitaxy of $MoSe_2$ on GaAs(111)A and (111)B, Cryst. Growth Des. **17**, 363 (2016).

[16] A. Ohtake and Y. Sakuma, Two-dimensional $WSe_2/MoSe_2$ heterostructures grown by molecular-beam epitaxy, J. Phys. Chem. C **125**, 11257 (2021).

[17] D. Pierucci, A. Mahmoudi, M. Silly, F. Bisti, F. Oehler, G. Patriarche, F. Bonell, A. Marty, C. Vergnaud, M. Jamet, H. Boukari, E. Lhuillier, M. Pala, and A. Ouerghi, Evidence for highly P-Type doping and Type II band alignment in large scale monolayer WSe_2/Se−terminated GaAs heterojunction grown by molecular beam epitaxy, Nanoscale **14**, 5859 (2022).

[18] M. T. Dau, C. Vergnaud, A. Marty, C. Beigné, S. Gambarelli, V. Maurel, T. Journot, B. Hyot, T. Guillet, B. Grévin, H. Okuno, and M. Jamet, The valley Nernst effect in WSe_2, Nat. Commun. **10**, 5796 (2019).

[19] Y. Zhang, M. M. Ugeda, C. Jin, S. F. Shi, A. J. Bradley, A. Martín-Recio, H. Ryu, J. Kim, S. Tang, Y. Kim, B. Zhou, C. Hwang, Y. Chen, F. Wang, M. F. Crommie, Z. Hussain, Z. X. Shen, and S. K. Mo, Electronic structure, surface doping, and optical response in epitaxial WSe_2 thin films, Nano Lett. **16**, 2485 (2016).

[20] W. Zhao, Z. Ghorannevis, K. K. Amara, J. R. Pang, M. Toh, X. Zhang, C. Kloc, P. H. Tan, and G. Eda, Lattice dynamics in mono- and few-layer sheets of WS_2 and WSe_2, Nanoscale **5**, 9677 (2013).

[21] R. H. Godiksen, S. Wang, T. V. Raziman, J. G. Rivas, and A. G. Curto, Impact of indirect transitions on valley polarization in WS_2 and WSe_2, Nanoscale **14**, 17761 (2022).

[22] A. Mahmoudi, M. Bouaziz, N. Chapuis, G. Kremer, J. Chaste, D. Romanin, M. Pala, F. Bertran, P. Le Fèvre, I. C. Gerber, G. Patriarche, F. Oehler, X. Wallart, and A. Ouerghi, Quasi van der Waals epitaxy of rhombohedral-stacked bilayer WSe_2 on GaP(111) heterostructure, ACS Nano **17**, 21307 (2023).

[23] See Supplemental Material at http://link.aps.org/supplemental/10.1103/PhysRevB.109.115437 for additional growth uniformity evidence, energy distribution curves at Γ and k points, and an extensive comparison between the experimental band structure of WSe_2/GaP(111) and DFT calculation from all possible stacking configurations. Supporting Information: Growth uniformity of trilayer WSe_2 phase. Energy distribution curve (EDC), obtained by integrating the intensity map in a wavevector window of 0.05 $Å^{-1}$ at Γ point confirming the trilayer signature. Comparison between the experimental band structure of WSe_2/GaP(111) and DFT calculation.

[24] I. C. Gerber, B. Chen, S. Alamdari, B. Urbaszek, X. Marie, G. Wang, T. Amand, S. Yang, S. Tongay, A. Suslu, and C. Robert, Spin-orbit engineering in transition metal dichalcogenide alloy monolayers, Nat. Commun. **6**, 10110 (2015).

[25] Z. B. Aziza, V. Zólyomi, H. Henck, D. Pierucci, M. G. Silly, J. Avila, S. J. Magorrian, J. Chaste, C. Chen, M. Yoon, K. Xiao, F. Sirotti, M. C. Asensio, E. Lhuillier, M. Eddrief, V. I. Fal'ko, and A. Ouerghi, Valence band inversion and spin-orbit effects in the electronic structure of monolayer GaSe, Phys. Rev. B **98**, 115405 (2017).

[26] N. R. Wilson, P. Rivera, A. J. Marsden, N. D. M. Hine, P. V. Nguyen, G. C. Constantinescu, N. R. Wilson, V. Kandyba, D. H. Cobden, K. Seyler, A. Barinov, Z. P. L. Laker, and X. Xu, Determination of band offsets, hybridization, and exciton binding in 2D semiconductor heterostructures, Sci. Adv. **3**, e1601832 (2017).

[27] C. Ernandes, L. Khalil, H. Henck, M. Q. Zhao, J. Chaste, F. Oehler, A. T. Charlie Johnson, M. C. Asensio, D. Pierucci, M. Pala, J. Avila, and A. Ouerghi, Strain and spin-orbit coupling engineering in twisted WS_2/Graphene heterobilayer, Nanomaterials **11**, 2921 (2021).

[28] D. R. Hamann, Optimized norm-conserving Vanderbilt pseudopotentials, Phys. Rev. B **88**, 085117 (2013).

[29] J. P. Perdew, K. Burke, and M. Ernzerhof, Generalized gradient approximation made simple, Phys. Rev. Lett. **77**, 3865 (1996).

[30] J. Heyd, G. E. Scuseria, and M. Ernzerhof, Hybrid functionals based on a screened Coulomb potential, J. Chem. Phys. **118**, 8207 (2003).